Semi-Analytical Methodology for Fretting Wear Evaluation of Unlubricated Pitch Bearing Raceways Under Operative and Non-Operative Periods

David Cubillas [1], Mireia Olave [1], Iñigo Llavori[2], Ibai Ulacia [2], Jon. Larrañaga [2], Aitor Zurutuza [3], Arkaitz Lopez[3]

[1]Ikerlan Technology Research Centre, Basque Research and Technology Alliance (BRTA). Pº J.M. Arizmendiarrieta, 2. 20500 Arrasate/Mondragón. Spain.
[2]Mondragon Unibertsitatea - Faculty of Engineering, Loramendi 4, 20500, Arrasate-Mondragon, Spain
[3]Laulagun Bearings, Harizti Industrialdea 201-E 20212, Olaberria, Spain.

Correspondence to: D. Cubillas (dcubillas@ikerlan.es)

Abstract. Current methodologies for the evaluation of fretting in pitch bearing raceways only consider damage induced by oscillating control movements. However, pitch bearings can remain static for long operative and non-operative periods, where load fluctuations cause fretting damage due the small movements and deformations at the contact. In this work a semi-analytical methodology is presented and an analysis of the fretting phenomenon in pitch bearing raceways in the absence of lubricant under both productive and non-productive periods of static pitch control is accomplished. The analysis is performed following the energy-based wear model and the calculation of a total 30 times series of 10 minutes of duration concerning winds speeds from 3 m/s to 25 m/s. As result, critical locations based on the dissipated energy are identified for the different wind speeds, the contribution of operational and non-operational times are evaluated independently and compared, as well as the prediction of damage shapes on the raceway for both cases.

1 Introduction

Wind industry has remarkably grown over the last decades compared to the general industry due to the high demand of clean and renewable energy (Nematollahi et al., 2016) (Rodríguez et al., 2019). This fact has been accompanied by new advances in design, materials and manufacturing techniques that finally have resulted in wind turbines of larger dimension, and consequently, larger components (Serrano et al., 2016). This fact and the extreme operational conditions have led to complex scenarios where the methodologies for common components are not reliable. While new calculation procedures and design guidelines have been proposed for the analysis of the reliability of the pitch bearing raceway in terms of rolling contact fatigue and fretting damage, these techniques are supported by simple methods or high safety factors that generally result in conservative calculus, and a low design optimization (Harris et al., 2009; Stammler et al., 2024; Portugal et al., 2017; Houpert, 1999; Schwack et al., 2016; Heras et al., 2017; Olave et al., 2010; Lopez et al., 2019). This fact has promoted the usage of experiments to test the reliability of the wind turbine components under their different failure modes (Stammler and Geibel,

2024; Stammler et al., 2019; Menck et al., 2020; Schwack et al., 2021). This technique has been applied to the real scale components, and therefore, it has provided effective and reliable results. However, it implies high costs due to the need of real scale components, materials, and equipment, that are even increasing due to the continuous component growth. This raises the need for design methodologies and scaled testing approaches whose results are valid for real scale applications (Olave et al., 2019).

Pitch bearings are typically large 4-point contact ball (4PCB) bearings, they link the blades to the hub and allow pitch control to locate the blade in the optimal position to maximize lift of the airfoils and to reduce the structural loads when the wind is too high (Bossanyi, 2003). Due to the pitch control strategy, these bearings usually oscillate and, eventually, the amplitude of the movement can be low enough (Harris et al., 2009.) to result in rotational fretting at the bearing raceway (Schwack et al., 2016; Wandel et al., 2023; Stammler et al., 2019) as consequence of the reciprocating rolling motion of the balls (Cai et al., 2020) and the evacuation of the lubricant out of the contact between the rolling element and the raceway. The fretting damage is also known as standstill marks (small amplitudes, $x/2b<1$), or false brinelling (small amplitudes, $x/2b>1$) (Presilla et al., 2023) . This phenomenon has been extensively studied for different authors where analytical (Cubillas et al., 2022), numerical (Schwack et al., 2018; Lin et al., 2022) and experimental (Grebe et al., 2011; Grebe et al., 2020; Schwack et al., 2021) (Pittroff, 1961; Stammler, 2023) methods have been used to study the effects of these control movements on the fretting damage. As result, it has been concluded that oscillatory movements of enough amplitude promote the relubrication of the raceway and aid to avoid fretting damage. Therefore, the premeditated use of the control movements, called protection runs, have been experimentally studied to observe their effects on the damage to avoid damage (Stammler et al., 2019).

Under some circumstances, such as, pre-commissioning, low wind speed or safe operating stops, pitch control can remain static for large periods of time. Under this scenario, pitch bearing still must accommodate tilting moments exerted by the wind and the blades weight that are transmitted between the rings through the balls. As consequence, balls experience variable loads what may cause radial fretting (Zhu et al., 2006; Cubillas et al., 2021), and additionally, this variable load causes small deformations at the ball and the rings contact that result in small rolling movements (Olave et al., 2010) in the transversal direction of the raceway that squeeze out the lubricant and, finally, they may cause rotational fretting.

Despite of the invested efforts in literature on the analysis of the pitch control moments on pitch bearing raceway, the effect of the variable loads when the pitch control remains static have not been studied. In previous work, the authors have developed and validated formulations for the analysis of radial fretting (Cubillas et al., 2021), rotational fretting (Cubillas et al., 2022) and the combination of both (Cubillas et al., 2022) in small bearings.

The objective of this work is to propose a methodology to analyze the relative contributions of productive and non-productive periods of wind turbine operation to pitch bearing fretting damage, including identification of the most likely location of damage on each raceway. For this task, the 5MW NREL reference wind turbine has been taken as case of study, and a total 30 time series of different design load cases (DLC) of normal production (DLC 1.2) and non-productive conditions periods (DLC 6.4) from IEC 61400-3-1 are evaluated through a wear energy-based model.

In this work, the damage evaluation has been addressed using energy-based wear models that have previously demonstrated
adequate correlation to damage (Brinji et al., 2020; Schwack et al., 2018; Cubillas et al., 2022). Although the present analysis
does not consider the effect of the lubricant, pitch bearings are likely to be in boundary lubrication conditions when the pitch
angle is not changing in non-operative periods and even in some low wind speed operations in which the model is valid.
Therefore, the authors believe that the proposed method provides a reliable framework for the prediction of the most critical
areas on the raceway where fretting damage can occur as well as a basis for comparison between the severity of different wind
speeds and operating conditions.

2 Methodology

In previous work (Cubillas et al., 2022), the authors developed and validated a complete methodology to predict fretting
damage in static angular bearing subject to variable loads. In this work, this methodology is extended and adapted to the 4PCB
bearing problem.

Figure 1 shows the flowchart of the complete methodology. The required inputs are the wind time series containing the value
of the bearing reaction along the time $M_x(t)$, $M_y(t)$, and the geometry. The maximum value of the bearing reaction and the
geometry are used to perform an design of experiments FEM simulations that determines a surface response with the values
of every ball reaction and contact angle as function of the bearing reaction, ball id (i=1: z), row (j=1:2), and contact id (k=1:4),
see Figure 2.

Once the response surface is created, it is possible to calculate the contact reaction, $Q(t)$, and the contact angle, $\alpha(t)$, of every
contact point of a ball in a specific time, then the contact reaction provides the enough information to calculate the contact
deformations; and the variation in the contact angle allows to determine the ball motion. The kinematics of the ball are
calculated following author´s previous work (Cubillas et al., 2022), with an iterative solver for rolling friction minimization.
This is implemented using the Nelder-Mead simplex algorithm, as described in (Lagarias et al., 1998), with a tolerance on the
function value of 10e-4. Within this iterative solver the local rigid slip, tangential stresses, and sliding are calculated. Finally,
the fretting damage and the probability of damage initiation are calculated. Each of these steps are described in the following
subsections.

2.1 Wind turbine: 5MW NREL reference turbine

For the analysis purpose, the 5MW NREL case of study has been selected (Jonkman et al., 2009). This model is a utility-scale
multimegawatt turbine, conventionally three-bladed and variable blade-pitch-to-feather-controlled. It has been used as a
reference turbine by research teams throughout the world to standardize baseline offshore wind turbine specifications and to
quantify the benefits of advanced land- and sea-based wind energy technologies (Zuheir et al., 2019; Cherubini et al., 2021;
Halawa et al., 2018).
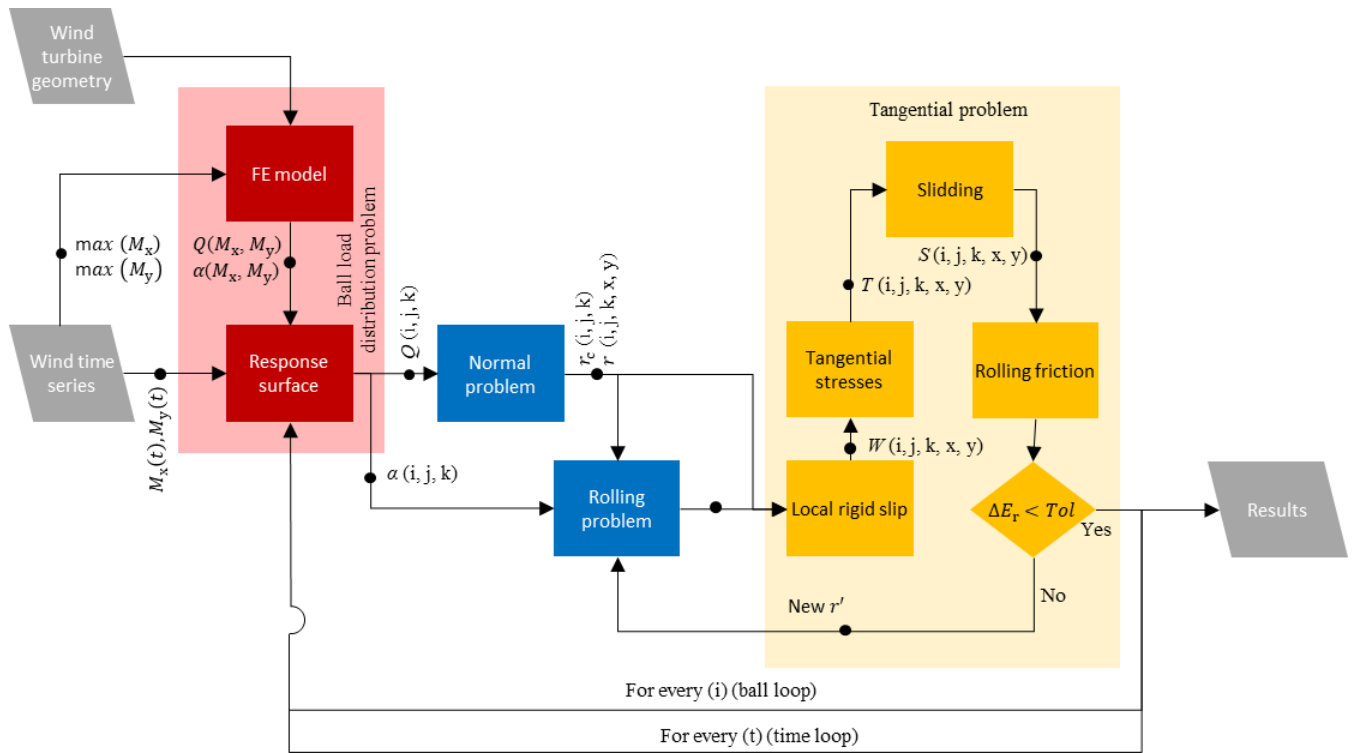
Figure 1: Flow chart of the proposed semi-analytical formulation showing the necessary calculation process with the involved loops to calculate the fretting damage where the suffix i defines the number id of the ball, the suffix j defines the row id, the suffix k defines contact location, and the suffix t defines the time step, Q is the normal load over a contact, α is the contact angle, r_c is the contact deformed radius, r is the distance from a contact point to the rolling axis, r' is the effective rolling radius, W is the local rigid slip, T is the tangential stresses, S is the local sliding and E_r is the rolling energy.
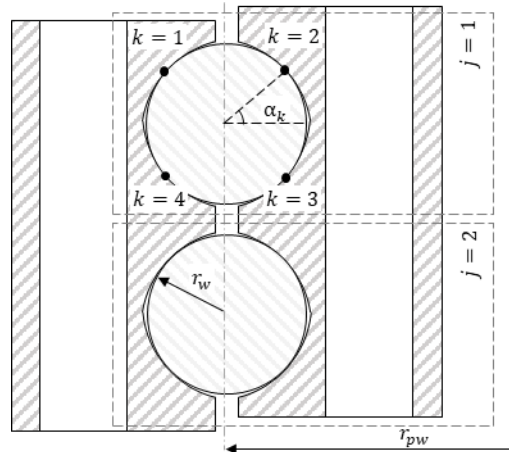
Figure 2: Generic 4PCB bearing of pitch radius d_{pw}, ball radius r_w, and the definition of the contact through the suffix j that defines the id of the row, and the suffix, k, that defines the id of the contact location.

105   Bearing case of study is a double row 4PCB bearing attached to the hub and the blade through bolts. Table 1 summarises the value of the main parameters of the bearing.

Table 1. Bearing geometrical characterises.

Bearing dimensions			
d_{pw}	Bearing pitch diameter	3610.0	[mm]
r_w	Ball radius	32.50	[mm]
c_O	Conformity	0.52	[-]
D_s	Bolts diameter	36.00	[mm]
H	Bearing ring height	200	[mm]
B	Bearing ring width	200	[mm]
z	Number of balls	121	[-]

2.2 Pitch control and time series

Pitch control is usually Collective Pitch Control (CPC) or Individual Pitch Control (IPC) (Lopez et al., 2019). While CPC
110   defines the position of the blades simultaneously, the IPC defines the position of each blade individually. Both controls result in oscillating movements, and beside of this classification, the final routines of oscillations can be as specific as the turbine design, the world location, and the climate conditions. For this work, a reference control with 5 seeds of wind time series of the normal turbulence model (NTM) from winds of 3 m/s to 25 m/s according to the design load cases (DLC) (61400-3, 2009) DLC1.2 (normal production) and DLC 6.4 (parked turbine with idling rotor) are available with an individual duration of 10
115   minutes at 20Hz. Figure 3 shows the evolution of the power production with the wind speed, and the value of the pitch bearing angle rate where the pitch control remains static for values under 7 m/s.
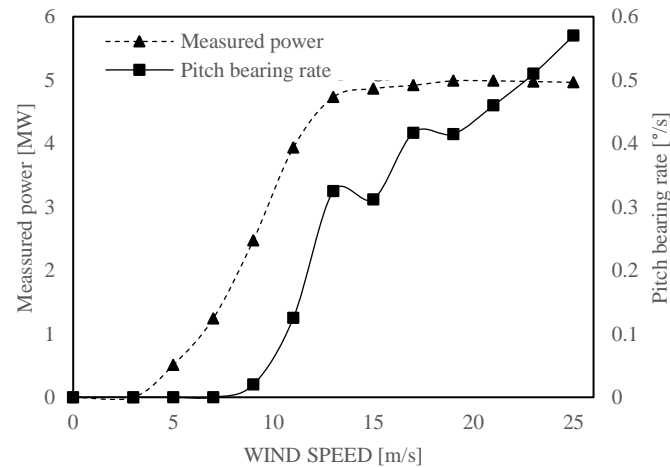
Figure 3: Pitch control performance of the 5MW NREL reference wind turbine as function of the wind to maximum 25 m/s speed and the measured power (Lopez A. et al., 2019).

120   Following above observations, only series under 7 m/s are considered from DLC 1.2, series of 3 m/s, 5 m/s, and 7 m/s, and all available series from DLC 6.4, series of 3 m/s, 11 m/s and 25 m/s. The aeroelastic wind time series are decomposed in bearing reactions using the software BLADED (DNVGL-ST-0437, 2016).

2.3 Ball load distribution and contact angle problem

    As described, in (Cubillas et al., 2022), a finite element (FE) model is necessary to calculate the contact reaction, Q, and the
125   contact angle, α, of every contact of every ball under a specific bearing load scenario.

$$Q = f(M_x, M_y, i, j, k), \tag{1}$$

$$\alpha = f(M_x, M_y, i, j, k), \tag{2}$$

    However, this method is time consuming, and the calculation of every time increment of the time series is not practical. To manage this inconvenience, an experiment design is accomplished covering all possible load cases (see Table 2) that allows for creation of a response surface. Radial forces and axial forces are neglected in this analysis as it has been demonstrated not to have a considerable effect on the bearing load distribution (Portugal et al., 2017). A total 8 simulations are performed where
130   the load is gradually applied in 10 load increments resulting in a total 80 load cases.

Table 2. DoE for the development of a surface response of the contact reaction and contact angle.

Id	1	2	3	4	5	6	7	8
Mx	M_x^{Max}	M_x^{Max}	0	M_x^{Min}	M_x^{Min}	M_x^{Min}	0	M_x^{Max}
My	0	M_y^{Max}	M_y^{Max}	M_y^{Max}	0	M_y^{Min}	M_y^{Min}	M_y^{Min}

    The FE model is built in ANSYS considering not only the bearing geometry but also the geometry of the blade, bolts, and stiffeners. Nevertheless, a symmetric behaviour is assumed and only one blade and 1/3 of the hub is considered, see Figure 4a.
135   It is important to mention that the results in the areas around the circumference may be affected by this assumption by not considering the cross effects at the root of the blade. Bearing, and stiffeners are structural steel, hub is cast iron and, in the absence of a realistic blade design to carry out the calculation, a laminate circular tube with constant section equal to the bearing ring has been incorporated to apply a geometric offset where the force can be applied. Table 3 summarizes the elastic properties of the mentioned materials.

140   **Table 3. Elastic properties of the wind turbine components**

Property	Cast iron	Struct. steel	Lam.	Units
Elastic module	210	110	40	[GPa]
Shear module	76.9	42.9	15	[GPa]
Poisson ratio	0.3	0.28	0.3	[ ]

The entire mesh is composed of second order elements and a total 1562761 elements are used in the entire model with a maximum value of the element size of 10 mm in the bearing. Balls are replaced by two linear elements with variable stiffness connected to both bearing raceways (Daidié et al., 2008). To get this aim, rectangular partitions along the bearing raceway of

145   dimensions a_{max}, b_{max}. In these partitions, an ordered mesh of 2x8 elements is generated and this is fixed to the end of the linear element at its opposite point as seen in Figure 4c. Analogously, bolts are replaced by linear elements considering the minimum section see Figure 4b.

Moment is applied through a remote point located at bearing centre and linked to the blade with a flexible behaviour. In this way, the decomposition of the moment is prevented, and a true moment is ensured. Attending to the previous assumption of

150   symmetric behaviour of the hub, frictionless supports are applied to the cut surfaces to prevent normal deformations and allow deformations along the symmetry plane. Frictional contacts are used at the contacts between the bearing rings, stiffeners, and blade with a 0.3 coefficient of friction with asymmetric behaviour and augmented LaGrange formulation. Bolts extremes are connected to the bearing rings, blade, and hubs with a multi-point constraint contact (MPC) contact, and a 608 kN of pretension is applied to the bolts based on a 10.9 grade.
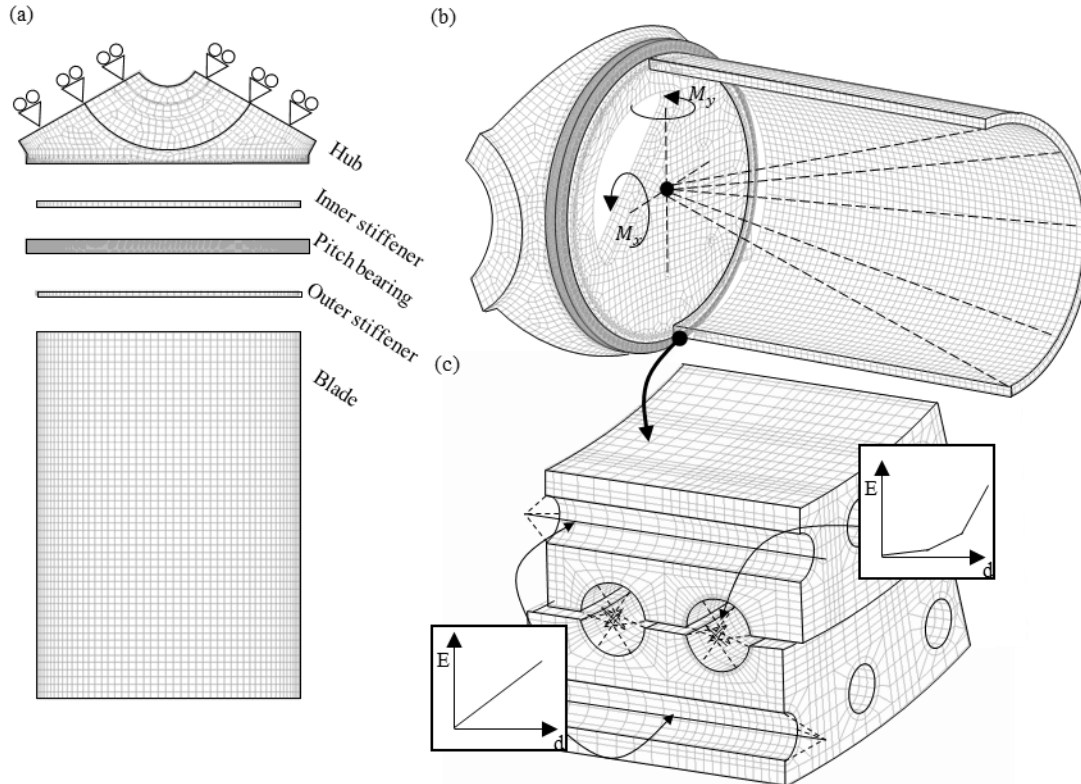
155

Figure 4: FEM model of the 5MW NREL reference wind turbine formed by the hub, the pitch bearing, the blade, and the inner and outer stiffeners; (a) Simplification of the original geometry considering a symmetric behaviour of the hub; (b) Application of the tilting moments through a remote point located at the bearing centre;(c) Detail of the bearing mesh and the simplifications of balls and bolts by a spring with non-linear and linear behaviour respectively.

2.4 Contact problem

Brewe and Hamrock formulation (Brewe and Hamrock, 1977) can be used to define contact area through the mayor and minor ellipse axis, a and b, respectively (see Figure 5a):

$$a = a^* \cdot \left(\frac{3 \cdot Q_{ijk} \cdot (1 - v^2)}{S_{ijk} \cdot E} \right)^{1/3}, \tag{3}$$

$$b = b^* \cdot \left(\frac{3 \cdot Q_{ijk} \cdot (1 - v^2)}{S_{ijk} \cdot E} \right)^{1/3}, \tag{4}$$

where, E is the elastic modulus of the material, v is the Poisson´s ratio, S_{ijk} is the sum of the contact curvatures of the groove curvature at row j and raceway k, N_{ijk} is the normal load at the ball i, row j and contact k, and a^* and b^* are the dimensionless semiaxes quantity of the mayor and minor semiaxes respectively. APPENDIX A describes the calculation of the above variables.

Additionally, both bearing raceway and ball deform to finally coincide in a transversal curvature (Hertz, 1882), r_c:

$$r_c = \frac{2 \cdot r_w}{1 - s} \tag{5}$$

2.5 Transversal rolling problem

Following our previous work (Cubillas et al., 2022), the travelled distance of the ball through the raceway, Δx, (see Figure 5a) can be calculated as:

$$\Delta x = \Delta \alpha \cdot r_c, \tag{6}$$

and the creepage, ε, is calculated as:

$$\varepsilon_x = \frac{r - r'}{r'}, \tag{7}$$

where, r' is the effective radius (calculated in the iterative process of energy minimization) and r is the distance from any point to the rolling axis:

$$r\,(x, y) = \sqrt{r_c^2 - x'^2} - \sqrt{r_c^2 - a(y')^2} + \sqrt{r_w^2 - a(y')^2}, \tag{8}$$

where, x' and y' are the local coordinates of the ball according to Figure 5a, $a(y)$ is the distance from a point to the ellipse bound in x direction, and $b(x)$ is the distance from a point to the ellipse bound in y' direction. Both can be calculated respectively as:

$$a(y') = \sqrt{a^2 \cdot \left(1 - \frac{y'^2}{b^2} \right)}, \tag{9}$$

$$b(x') = \sqrt{b^2 \cdot \left(1 - \frac{x'^2}{a^2}\right)}, \tag{10}$$

2.6 Tangential friction problem

Following Kalker (Kalker, 1981), the relative motion of two points, $\vec{S}$ (local slip), can be decomposed in the rigid displacements, $\vec{W}$ (local rigid slip), and the elastic displacements, $\vec{U}$ (local elastic slip):

$$\vec{S} = \vec{W} - \vec{U}, \tag{11}$$

180 Considering an initial condition of no slip, then, the local elastic slip is equal to the local rigid slip:

$$\vec{S} = 0 \rightarrow \vec{U} = \vec{W}, \tag{12}$$

(a)   (b)
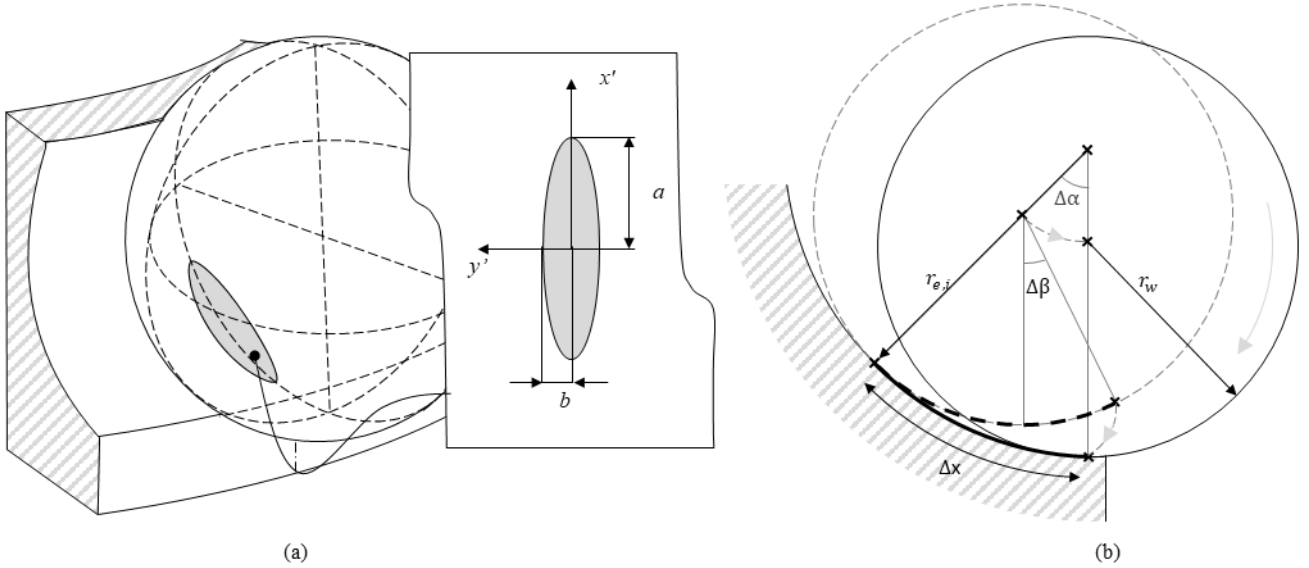
Figure 5: Contact area and rolling motion of the ball. (a) Definition of the elliptical contact area through the mayor ellipse semiaxes a, and the minor semiaxes, b, and the local coordinates y' aligned with the longitudinal direction of the raceway and x' aligned with the transversal direction of the raceway; (b) description of the rolling motion of the ball in the raceway transversal direction

185 Following step is to determine the local rigid motion at the contacting points:

$$\vec{W}(W_{x'}, W_{y'}) = W_{i,j,k}^{NL}\left(W_x^{NL}, W_y^{NL}\right) + W_{i,j,k}^{Ro}\left(W_x^{Ro}, W_y^{Ro}\right), \tag{13}$$

where, W^{NL} is the local rigid slip caused by the variable normal load, W^{Ro} is the local rigid slip caused by the rolling effects. According to our previous work (Cubillas et al., 2021), the local rigid slip caused by the normal load is calculated as:

$$W_x^{NL} = r_c \left(\tan^{-1}\left(\frac{x'}{\sqrt{r_p^2 - x'^2}} \right) \frac{\tan^{-1}\left(\frac{a(y')}{\sqrt{r_c^2 - a(y')^2}} \right)}{\tan^{-1}\left(\frac{a(y')}{\sqrt{r_p^2 - a(y')^2}} \right)} - \tan^{-1}\left(\frac{x'}{\sqrt{r_b^2 - x^2}} \right) \frac{\tan^{-1}\left(\frac{a(y')}{\sqrt{r_c^2 - a(y')^2}} \right)}{\tan^{-1}\left(\frac{a(y)}{\sqrt{r_w^2 - a(y')^2}} \right)} \right) \tag{14}$$

$$W_y^{NL} = r_c \left(\tan^{-1}\left(\frac{y'}{\sqrt{r_b^2 - y'^2}} \right) \frac{\tan^{-1}\left(\frac{b(x')}{\sqrt{r_c^2 - b(x')^2}} \right)}{\tan^{-1}\left(\frac{b(x)}{\sqrt{r_w^2 - b(x')^2}} \right)} - y \frac{\tan^{-1}\left(\frac{b(x')}{\sqrt{r_c^2 - b(x')^2}} \right)}{b(x)} \right), \tag{15}$$

On the other hand, the local rigid slip caused by the rolling motion considering the transient phenomena (Al-Bender & De Moerlooze, 2008) can be calculated as:

190   If $a(y') - \Delta x \leq x$ and $x < a(y')$:

$$Wx_{Rx} = \varepsilon \cdot (x' - a(y')) \tag{16}$$

If $a(y') - \Delta x' > x'$ and $x' \geq -a(y')$:

$$Wx_{Rx} = \varepsilon \cdot \Delta x' \tag{17}$$

2.7 Tangential stresses, sliding, and rolling energy

Kalker simplified theory (Kalker, 1982) is applied to determine the tangential stress $\vec{T}$:

$$\vec{T}(x', y') = \frac{\vec{W}(x', y')}{L}, \tag{18}$$

where, L is the flexibility parameter calculated as:

$$L = \frac{8 \cdot a}{3 \cdot C \cdot G} \tag{19}$$

195   where, G is the shear modulus, and C is the creepage coefficient. The creepage coefficient is tabulated in [56] as a function of the Poisson's ratio and the contact area; however, for the numerical implementation of the method, a polynomial regression was taken from the tabulated values:

$$C = -1.60 \cdot 10^{-3} \cdot \left(\frac{a}{b} \right)^3 + 1.08 \cdot 10^{-2} \cdot \left(\frac{a}{b} \right)^2 + 0.89 \cdot \left(\frac{a}{b} \right) + 3.44 \tag{20}$$

However, tangential stresses must be reconsidered at those points where slip occurs, if $T(x, y) > \mu \cdot P(x, y)$:

$$T(x', y') = \mu \cdot P(x', y') \tag{21}$$

$$U(x', y') = \mu \cdot P(x', y') \cdot L \tag{22}$$

where, μ is the value of the coefficient of friction (CoF), and P is the contact pressure:

$$P(x',y') = \frac{3 \cdot Q}{2\pi \cdot a \cdot b} \cdot \sqrt{1 - \left(\frac{x'}{a}\right)^2 - \left(\frac{y'}{b}\right)^2} \tag{23}$$

then, reconsidering (11), the local slip:

$$S(x,y) = W(x,y) - U(x,y) \tag{24}$$

Finally, the rolling energy, E_R is calculated from the local terms:

$$E_{\mathrm{R}} = \iint S \cdot T_{\mathrm{l}} + U \cdot T \, dxdy \tag{25}$$

2.8 Fretting damage indicators

An energy based model has proposed and validated (Fouvry et al., 2003) for fretting applications, considering the dissipated friction energy where the wear volume, V_w, is proportional the total accumulated friction energy (TFE), E_F and the wear coefficient, k_w:

$$V_w = k_w \cdot E_{\mathrm{F}}, \tag{26}$$

where E_{F} is calculated from local terms as:

$$E_{\mathrm{F}} = \iint S(x',y') \cdot T(x',y') \cdot dxdy. \tag{27}$$

The dissipated energy can be also expressed as a distribution through the density of the accumulated friction energy (DFE), ρ_{F}:

$$\rho_{\mathrm{F}}(x',y') = S(x',y') \cdot T(x',y') \tag{28}$$

Then, both the dissipated energy, E_F, and its density, ρ_F, are instantaneous variables in local coordinate systems. To achieve the cumulative evolution of damage on the global coordinate system, these are translated into cumulative variables, the accumulated friction energy, TFE, and accumulated energy density, MDFE. Thus, considering the change in position due to the variation of the contact angle:

$$TFE = \int_0^t E_{\mathrm{F}}(t) \cdot \mathrm{d}t = \int_0^t \rho_{\mathrm{F}}(t) \cdot \mathrm{d}t \tag{29}$$

$$MDFE = \max\left(\int_0^t \rho_F(t) \cdot dt\right) \tag{30}$$

Following this work, multiple authors have found analogues result in multiple fretting wear applications, and in particular for false brinelling prediction in roller bearings (Fallahnezhad et al., 2019; Fallahnezhad et al., 2018; Brinji et al., 2021), angular bearings (Schwack et al., 2018), and thrust bearings (Cubillas et al., 2022; Cubillas et al., 2021). However, the value of k_w has shown dissimilar results as it is affected by multiple conditions such as frequency, sliding distance or pressure (Brinji et al., 2021), but also it will be greatly affected by lubrication conditions. Considering this fact and keeping in mind the objective of identifying critical areas and adverse behaviour, the damage assessment is done through energetic parameters only, TFE and MDFE.

3 Results and discussion

In this section the results from the simulations are presented. First, the load and contact angle distributions are studied to determine the areas that are exposed the most to variable loads and variable contact angles. Then, the distribution of the damage is analysed and compared to the load distribution to determine its effects on the final damage, and the effects of the wind; finally, the results of the probability of damage initiation are presented, and a cumulative model for variable winds analysis is proposed.

3.1 Load distribution and contact angles

Figure 6 shows the distribution of the mean and the amplitude load, the mean and the amplitude contact angle and the damage indicators, the total accumulated friction energy, TFE, and the maximum density of friction energy, MDFE, after the simulation of the total 15 wind series of 10 minutes of the DLC 1.2 and 6.4 respectively. For a clearer presentation of the results, contacts are classified attending to the load diagonal, the row, and the ring (inner and outer), and attending to the high number of contacting points and the similarity between adjacent locations, the results correspond to the mean value of two adjoining balls with the objective of facilitate the presentation of the data. Furthermore, considering the large difference between the damage values obtained in production and non-productive times, it has been decided to use different scales.

In this section, we first focus on the analysis of the loads and the contacts angles. The results show the presence of variable loads and rolling motion (as consequence of the variable contact angle), and therefore the potential presence of radial and rotational fretting damage. Previous classification into load diagonals, rows, and rings, allows to easily observe a same value of the mean and amplitude load and mean and amplitude contact angle at the inner and the outer rings as the contact reactions are equal in magnitude with opposite direction.

Means and amplitudes loads and contact angles show the expected symmetric behaviour respect to a crossing axis from 150º to 330º (see back dashed line in Figure 6). Also, the values of the mean load and the mean angle on one side, and the amplitude load and the amplitude angle on the other side, show some correlation. However, notable differences can be observed as the maximum values are not always located at the same angular position, and another interesting point is the dissimilar distribution between rows that can be observed through the maximum values at the row 1, and row 2, being significantly different. These facts show the important effect of the heterogeneous stiffness of the structure and endorse the usage of the FE model to calculate the bearing reactions as shown in (Olave et al., 2010). The distribution of the mean load with highest values located at D1 at 150º, and D2 at 315º shows the effect of a permanent tilting moment of similar components M_x and M_y attributed to the mean load exerted by wind. The highest values of the mean load are 30 kN for DLC 1.2 and 12 kN for DLC 6.4 at D1R2 and D2R1. Similarly, higher values of the mean angle can be found in close locations at 120° in D1 and at 320° in D2 with similar maximum mean values of 58º at D2R1 and D1R2 for the DLC 1.2 and 50° for the DLC 6.4. On the other hand, the results of the analysis of the DLC 6.4 show a more homogeneous distributed load over the bearing, where the lower value of the tilting
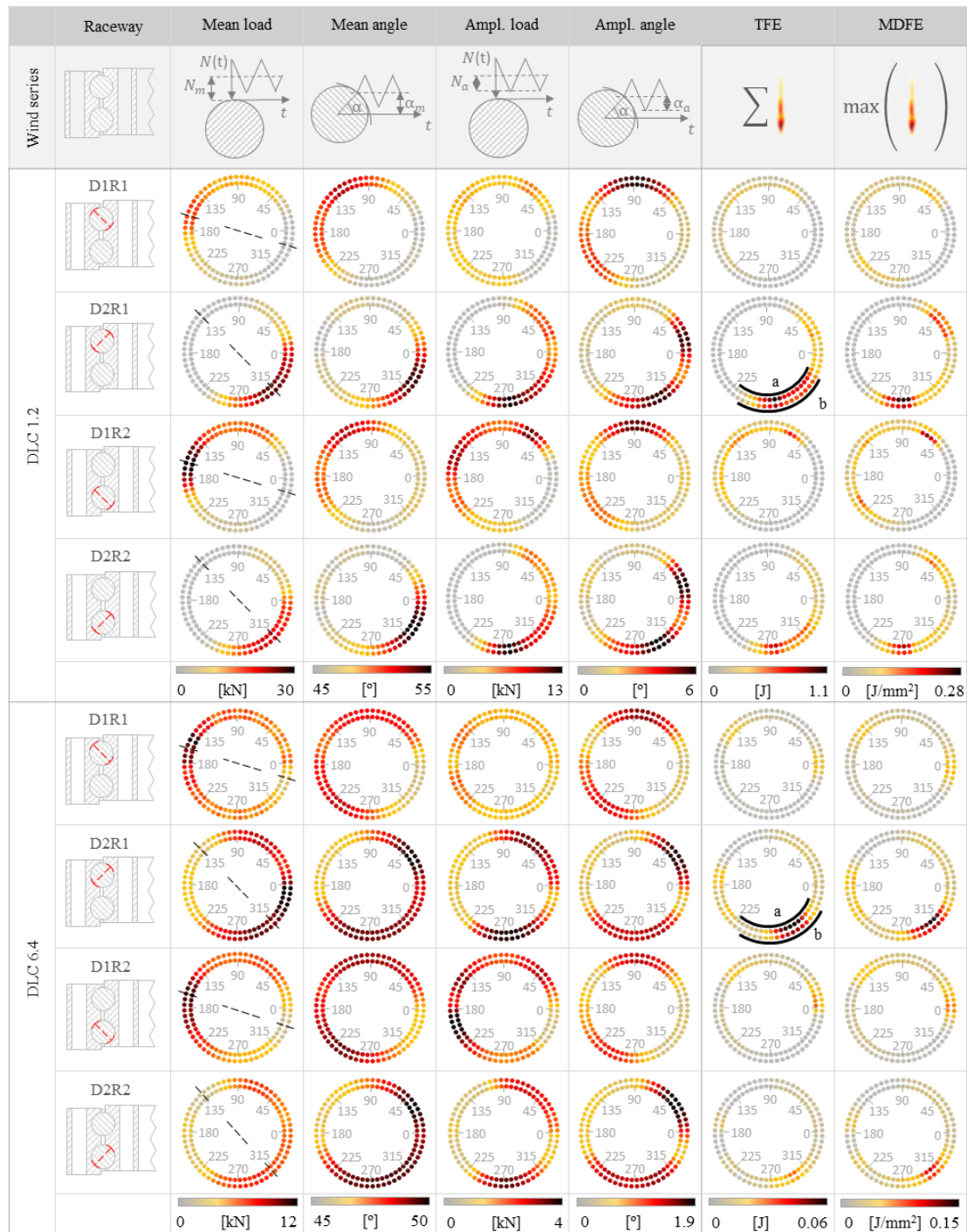
Figure 6: Summary of the results of the analysis of the mean load, amplitude load, mean angle, amplitude angle, the total dissipated friction energy (TFE) and the maximum value of the density of accumulated friction energy (MDFE) where results are classified attending to the row location, the load diagonal and for the different design load cases DLC 1.2 and 6.4

moment might amplify the effects of the heterogeneous stiffness resulting in different locations of the maximum values of the loads and the contact angles.

On the other hand, the higher values of the amplitude load are located at 60º, 150º and 225º in D1, and 30º and 270º in D2 with a maximum value of 13kN for the DLC 1.2 and 4 kN for the DLC 6.4. This distribution reveals the presence of a complex scenario with an alternative tilting moment of components Mx and My caused by the alternative load of the blade weigh due to the turbine movement, and the fluctuation of the wind. The regions of high variable load reveal critical regions for the occurrence of radial fretting. Similarly, the higher values of the amplitude of the contact angle can be found at 90◦ and 225º at D1, and 20º and 300º at D2 with a maximum value of 6º for the DLC 1.2 and 1.9º for the DLC 6.4 at D2R1. This regions of high amplitude of the contact angle indicates the presence of rolling motion of the balls, and consequently, they could be critical for the development of rotational fretting. The amplitude of the contact angle indicates the presence of rolling motion of the balls, and consequently, these regions are critical for the development of rotational fretting.

4.2 Damage indicators

In Figure 6, both damage indicators, the total accumulated friction energy, TFE and maximum density of friction energy, MDFE, show similar distribution of the damage being the TFE maximum at 60º, 135º, and 180º at D1, and at 30º and 275º in D2, and the MDFE at 275 in D2R1 for the DLC 1.2; and at 290º in D2R1 for the DLC 6.4. These damage distributions keep certain similarities with the mean and amplitude load distributions and the mean and amplitude angle pointed in the previous section. However, the correlation of the distribution of damage seems to hold the best fit with the distribution of the amplitude load. Therefore, results might indicate that the main source of damage is the radial fretting caused by the variable load of the wind and the blade weight dynamics. This fact is aligned with previous work (Cubillas et al., 2022) where the analysis of an angular bearing indicated that the 70% of the fretting damage caused for a variable load was produced by radial fretting. In addition, the TFE and the maximum value of the MDFE show damage distributions where the inner ring is significantly more damaged in all diagonals and rows. The value of TFE in the IR is from 1.8 to 4.6 times higher than the OR, and similarly, the value of the MDFE of the IR is from 1.2 to 3.6 times the OR. As described in previous section, the value of the contact reaction and the contact angle are equal in magnitude for the inner and the outer ring contact, therefore, no differences can be made in terms of load or motion, and consequently, the different damage can only be attributed to the different contact curvatures of the bearing raceway where the inner contact is convex respect to the longitudinal curvature (r_b vs r_{pw}), and concave respect to the transversal direction (r_b vs r_p), while the outer ring contact is concave respect to both transversal and longitudinal curvatures. Therefore, the increasing main diameter of the bearings would aid to balance the damage at the inner ring.

Figure 7 shows the density of the friction energy, ρ_F, along the different bearing raceways, being the axis x, the longitudinal direction of the raceway and the axis y the transversal direction, according to the local coordinate system of Figure 5. The plotted sectors correspond to the location of the maximum values at D2R1 from 225º to 320º denoted by the regions a and b for the DLC 1.2, and for the DLC 6.4 (see Figure 6). In order to facilitate the visualization, and comparison of the
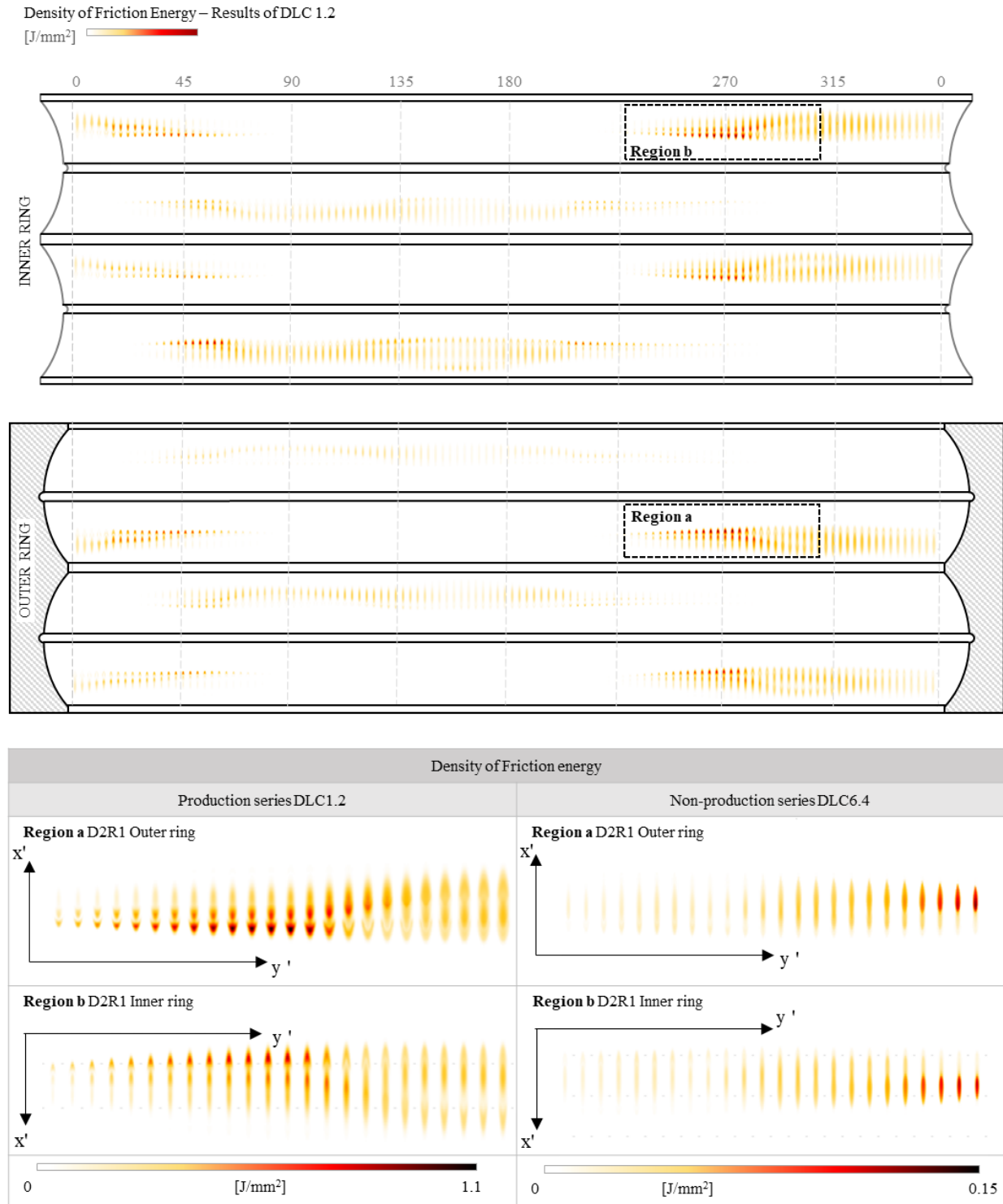
Figure 7. Density of dissipated friction energy, ρ_F, at regions a and b, according to Fig 5.

damage between adjacent ball damages, the distance between marks was reduced. The results show notable differences in the damage shapes for every contact where some look similar to the previous experimental results (Cubillas et al., 2022). All marks can be bounded in an elliptical area which is notable more rounded at the OR and more flattened at the IR what, as previous mentioned, is directly influenced by the contact curvatures of the rings. The forms of damage are significantly different for DCL1.2 and DCL6.4. In the case of DCL1.2 there are two intensity zones within each footprint, a central, elliptical zone and a horseshoe-shaped zone at the rear of the tread. In contrast, the DCL6.4 damage shows only one damage zone in the rear of the elliptical shaped tread. This fact may be related to the non-linear stiffness and how it affects the load ratio and contact angle. That is, for low loads, the contact is less stiff in relative terms as an increase in load results in an increase in contact angle. As the load increases, the stiffness of the contact is greater, and the change in contact angle is smaller, and therefore the rolling is less. Under these conditions the contribution from radial fretting damage, generated by the pulsating load, and rotational fretting damage changes.

4.3 On the effect of the wind speed

Figure 8 shows the results of the contribution of different wind speeds: 3 m/s, 5 m/s and 7 m/s of the DLC 1.2 and 3m/s 11m/s and 25 m/s of the DLC 6.4 to the total accumulated friction energy, TFE, in different wind speeds: 3 m/s, 5 m/s and 7 m/s of the DLC 1.2 and 3m/s 11m/s and 25 m/s of the DLC 6.4, unlike the previous where the sum of the contribution of each of them was presented. Due to the similarities of the damage distribution for both indicators, the TFE and the maximum density of friction energy, MDFE, only the results of the TFE are presented. According to previous sections, the results are also classified by the load diagonal, row, and ring.

As mentioned, the results of the contribution of different wind speeds: 3 m/s, 5 m/s and 7 m/s of the DLC 1.2 and 3m/s 11m/s and 25 m/s of the DLC 6.4. As it can be observed, a similar distribution of the dissipated energy where the location of the damage seems not to be affected by the wind speed and the maximum values can be found at 60º, 135º, and 190º at D1, and at 30º and 270º in D2. Therefore, it can be concluded that the position of the critical zones is not dependent on wind speed. If the wind speed does not alter the location of the damage, it seems that the contribution of the fluctuating wind load is low. Therefore, it can be inferred that the main source of damage is caused by the swinging of the blade weight when the rotor is in motion.

While the location of the damage are invariant, a notable and expected effect of the wind speed is observed on the value of the value of the TFE where the results show a growing tendency of the dissipated energy with the increasing wind speed. Figure 9 shows the normalized value of the maximum TFE and the MDFE for the different wind speeds. Despite of the analogous growing tendency on both indicators with the growing wind speed, the tendency is significantly different: while the TFE has an exponential growth, the MDFE shows a logarithmic tendency. Considering that the TFE indicator refers to a global term after integrating local damage, i.e., it is a parameter that takes into account the total damaged area. While the MDFE is a local parameter, and it takes into account the intensity of damage at a given point. Therefore, the different trends of the two damage parameters indicate different effects. The MDFE indicates that the damage intensity grows logarithmically with wind speed,

while the TFE parameter secondarily and taking into account that the MDFE grows logarithmically, shows that the damaged area grows exponentially.

TFE	DLC 1.2			DLC 6.4		
	3 m/s	5 m/s	7 m/s	3 m/s	11 m/s	25 m/s
D1R1						
D2R1						
D1R2						
D2R2						
TFE	0 0.15 0.30 0.45 0.60 [J]			0.00 1.50 3.00 4.50 6.00 x10⁻³ [J]		
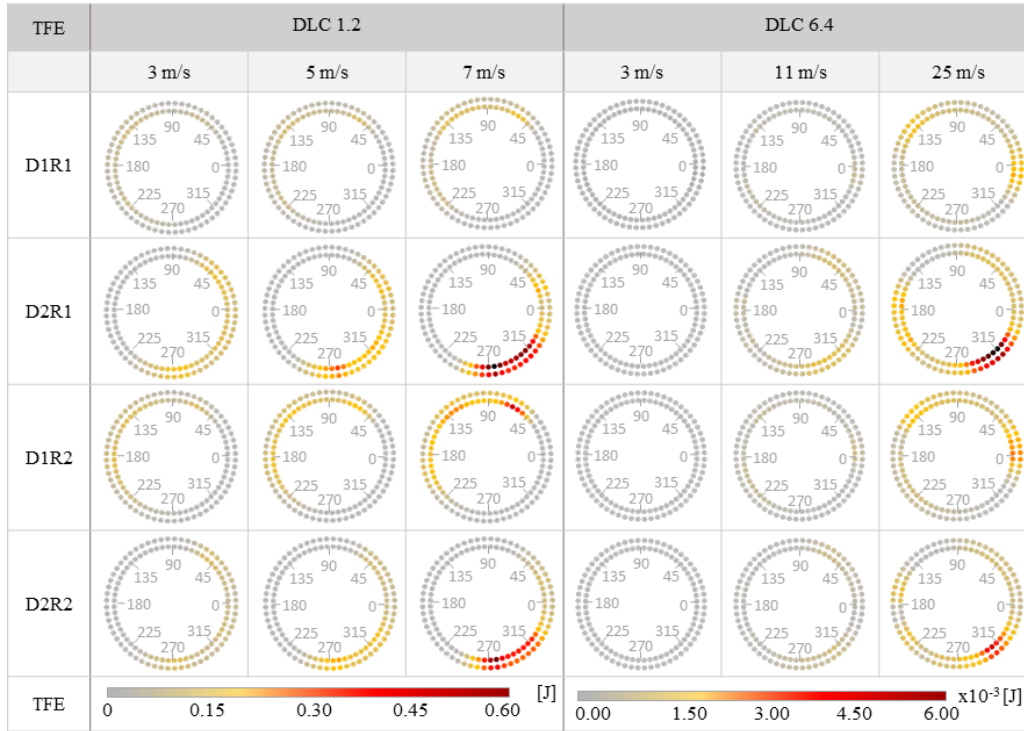
325 **Figure 8: Results of the total dissipated friction energy for different wind speeds of the design load cases DLC12 and DLC64 of 10 minutes of duration, where results are organized by load diagonal and row.**

a)   b)
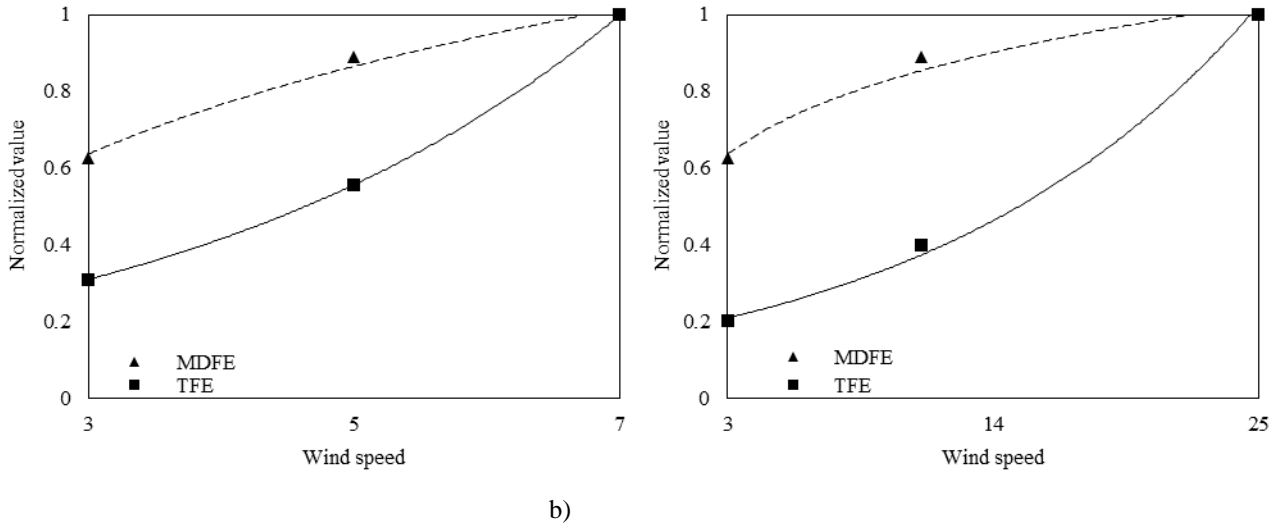
Figure 9: Evolution of the normalized values of the maximum density of friction energy MDFE and the total dissipated friction
330 **energy TFE as function of the wind speed, and the logarithmic and exponential regressions, respectively. a) Design load cases DLC 1.2; (b) Design load cases DLC 6.4.**

5 Conclusions

This work started with the aim to analyse the performance of fretting damage on productive and non-productive periods of pitch bearings under realistic time series and determine the critical locations and conditions that favoured the development of the damaged. As result, following conclusions have been taken:

- The energy-based wear model shows a critical region between 270º to 315º of the inner ring and at the first row where the total accumulated friction energy (TFE) and the maximum value of the density of friction energy (MDFE) are located in both, operational and no operational conditions.

- An analysis of the loads and contact angle distribution shows a noticeable better correlation between the friction energy and the variable load than the variable angle, and consequently, this implies that radial fretting is the main source of damage.

- The evaluation of the effects of the wind speed on the damage shows a similar distribution of the damage where maximum values remain at the same position. Therefore, the critical locations do not vary with the intensity of the wind. However, important differences are found in the value of the accumulated energy indicators that show an exponential behaviour of the TFE, and a logarithm trend of the MDFE as function of the wind speed. Therefore, the intensity of the damage is expected to be exponential with the wind speed.

- For time series of the same duration, the damage intensity obtained in productive times associated with the DLC 1.2 series is much higher than in the DLC6.4 series. Consequently, the productive times are much more critically affected by damage development.

- The results obtained in this work put light on the fretting damage mechanism in pitch bearings under different conditions of wind and operation. However, there is still a long way to go. Among these tasks, the most obvious would be to validate the proposed methodology on a real scale, with and without lubrication to see the validation framework, as well as the need to implement additional formulations for modeling the effect of grease. Additionally, the formulation should be extended to the prediction of wear over time, making the methodology usable as a prediction tool for design.

Acknowledgments

This work was partially supported by grant 20AFW2201900007 of the Bikaintek Program for the Completion of Industrial Doctorates and for the Incorporation of Researchers to the Industry from the Basque Government's Department of Economic Development, Sustainability and Environment.

The authors gratefully acknowledge the financial support given by the Eusko Jaurlaritza under 'Programa de apoyo a la investigación colaborativa en áreas estratégicas' (Project BISUM: Ref. KK-2021/00089).

Competing interests

The contact author has declared that none of the authors has any competing interests.

References

365 Al-Bender, F., and De Moerlooze, K.: A model of the transient behavior of tractive rolling contacts. Advances in tribology, https://doi.org/10.1155/2008/214894, 2008

Bossanyi, E. A.: Individual Blade Pitch Control for Load Reduction, 2003

Brewe, D., and Hamrock, B. J.: Simplified solution for elliptical- contact deformation between two elastic solids. Journal of Lubrication technology, 99(4), https://doi.org/10.1115/1.3453245, 1977

370 Brinji, O., Fallahnezhad, K., and Meehan, P.: Analytical model for predicting false brinelling in bearings, 444–445, https://doi.org/10.1016/j.wear.2019.203135, 2020

Brinji, O., Fallahnezhad, K., and Meehan, P.: False brinelling behaviour of high carbon bearing steel under varying conditions, https://doi.org/10.1016/j.wear.2021.203973, 2021

Byer, G., Bartschat, A., Wandel, S., B. S., and Poll, G.: Experimental Investigations on Wear in Oscillating Grease-Lubricated
375 Rolling Element Bearings of Different Size and Type, Lubricants, 2023.

Cai, Z., Yang, Z., Gui, M., Zhu, Y., and Zhou, Z.: A review of fretting study on nuclear power equipmen. 144, 2020

Cherubini, S., De Cillis, G., Semeraro, O., and Leonardi, S.: Data Driven Modal Decomposition of the Wake behind an NREL-5MW Wind Turbine, 2021

Cubillas, D., Olave, M., Llavori, I., Ulacia, I., Larranaga, J., Zurutuza, A., and Lopez, A.: A novel formulation for radial
380 fretting wear Application to false brinelling in thrust bearings, Wear. https://doi.org/10.1016/j.wear.2021.204078, 2021.

Cubillas, D., Olave, M., Llavori, I., Ulacia, I., Larranaga, J., Zurutuza, A., and Lopez, A.: An analytical formulation for rotational fretting: application to thrust bearings, Wear, 2021.

Cubillas, D., Olave, M., Llavori, I., Ulacia, I., Larranaga, J., Zurutuza, A., and Lopez, A.: Semi-analytical methodology to predict fretting damage areas in angular contact ball bearing raceways under variable loading, Wear, 508–509, 2021.

385 Daidié, A., Chaib, Z., and Ghosn, A.: 3D Simplified Finite Elements Analysis of Load and Contact Angle in a Slewing Ball Bearing. 130(8), 2008.

DNVGL-ST-0437, Loads and site conditions for wind turbines. (108), 2016.

Fallahnezhad, K., Liu, S., Brinji, O., Marker, M., and Meehan, P.: Monitoring and modelling of false brinelling for railway bearings. 424–425(151–164), 2019.

390 Fallahnezhad, K., Oskouei, R. H., and Taylor, M.: Development of a fretting corrosion model for metallic interfaces using adaptive finite element analysis,, 148, 2018.

Fouvry, S., Liskiewicz, T., Kapsa, P., Hannel, S., and Sauger, E.: An energy description of wear mechanisms and its applications to oscillating sliding contacts. 255(1–6), 2003.

Grebe, M., Feinle, P., and Hunsicker, W.: Various Influence Factors on the Development of Standstill Marks (False-Brinelling
395 Effect) (290–300), 2011.

Grebe, M., J. Molter, J., Schwack, F., and Poll, G.: Damage mechanisms in pivoting rolling bearings and their differentiation and simulation. June, 2020.

Halawa, A. M., Sessarego, M., Shen, W. Z., and Yoshida, S.: Numerical Fluid-Structure Interaction Study on the NREL 5MW HAWT. 1037(2), 2018.

400 Harris, T., Rumbarger, J. H., and Butterfield, C. P.: Wind Turbine Design Guideline DG03 : Yaw and Pitch Rolling Bearing Life, 2009.

Heras, I., Aguirrebeitia, J., and Abasolo, M.: Friction torque in four contact point slewing bearings: Effect of manufacturing errors and ring stiffness. 112(145–154), 2017.

Hertz, H.: Über die Berührung fester elastische Körper und über die Härte. (On the contact of rigid elastic solids and on
405 hardness). Verhandlungen des Vereins zur Beförderung des Gewerbefleisses, Leipzig, 1882.

Houpert, L.: Bearing life calculation in oscillatory applications. 42(136–143), 1999.

Jonkman, J., Butterfield, S., Musial, W., and Scott, G.: Definition of a 5-MW Reference Wind Turbine for Offshore System Development, 2009.

Kalker, J.: A Fast Algorithm for the Simplified Theory of Rolling Contact, 1981.

410 Kalker, J. J.: On the Rolling Contact of Two Elastic Bodies in the Presence of Dry Friction, 1093.

Kalker, J. J.: A Fast Algorithm for the Simplified Theory of Rolling Contact, 11, 1982.

Lagarias, J. C., Reeds, J. A., Wright, M. H., and Wright, P. E.: Convergence properties of the Nelder-Mead simplex method in low dimensions. 9(1), 1998.

Lin, C.-L., Fallahnezhad, K. B., and and Meehan, P. A.: Mitigation of False Brinelling in a Roller Bearing: A Case Study of
415 Four Types. Tribology letters, 2022.

Lopez, A., Zurutuza, A., Olave, M., Portugal, I., and Muniz-Calvente, M.: Pitch bearing lifetime prediction considering the effect of pitch control strategy. Journal of Physics, 1222(1). https://doi.org/10.1088/1742-6596/1222/1/012017, 2019.

Menck, O., Stammler, M., and Schleich, F.: Fatigue lifetime calculation of wind turbine blade bearings considering blade-dependent load distribution,. (1–19), 2020.

420 Nematollahi, O., Rasti, M., Hoghooghi, H., and Sedaghat, A.: Energy demands and renewable energy resources in the Middle East. Renew Sustain Energy Rev, 1172-81, 2016.

Olave, M., Sagartazu, X., Damian, J., and Serna, A.: Design of Four Contact-Point Slewing Bearing with a New Load Distribution Procedure to Account for Structural Stiffness, Journal of Mechanical Design, 132. https://doi.org/10.1115/1.4000834, 2010.

425 Olave, M., Sagartazu, X., Damian, J., and Serna, A.: Innteresting european project. https://www.Innterestingproject.eu.

Olave, M., Sagartzazu, X., Damian, J., and Serna, A. (2010). , "Design of Four Contact-Point Slewing Bearing With a New Load Distribution Procedure to Account for Structural Stiffness,. 132(2), (2019).

Pearson, S. R., and Shipway, P. H.: Is the wear coefficient dependent upon slip amplitude in fretting? 330–331(5).

Pittroff, H. (1961). Riffelbildung bei Wälzlagern infolge Stillstandserschütterungen, PhD thesis, Technische Hochschule
430 München, Munich, 2014.

Portugal, I., Olave, M., Zurutuza, A., López, A., Muñiz-Calvente, M., and and Fernández-Canteli, A.: Methodology to evaluate fatigue damage under multiaxial random loading. vol. 185(114–123), 2017.

Presilla, R., Wndel, S., Stammler, M., Grebe, M., Pall, G., and Glavatshkih, S.: Oscillating rolling element bearings: A review of tribotesting and analysis. Tribology International, 2023.

435 Ramalho, A., A, M., and Cavaleiro, A.: Fretting behaviour of W-Si coated steels in vacuum environments. 261(1), 2006.

Rodríguez, X. A., Regueiro, R. M., and Doldán, X. R.: Analysis of productivity in the Spanish wind industry. Renew. Sustain. Energy Rev, vol. 118, 2019.

Sauger, E., Fouvry, S., Ponsonnet, L., Kapsa, P., Martin, J. M., and Vincent, L.: Tribologically transformed structure in fretting. 245(1–2,), 2000.

440 Sauger, E., Ponsonnet, L., Martin, J. M., & Vincent, L.: Study of the tribologically transformed structure created during fretting tests. 33(11), 2000.

Schwack, F., Bader, N., Leckner, J., Demaille, C., and Poll, G.: A study of grease lubricants under wind turbine pitch bearing conditions. 454–455, 2020.

Schwack, F., Halmos, F., Stammler, M., Poll, G., and Glavatskih, S.: Wear in wind turbine pitch bearings—A comparative design study. (5–8), 2021.

Schwack, F., Prigge, F., and Poll, G.: Finite element simulation and experimental analysis of false brinelling and fretting corrosion, Tribology International, 126(352–362). https://doi.org/10.1016/j.triboint.2018.05.013, 2018.

Schwack, F., Prigge, F., and Poll, G.: Finite element simulation and experimental analysis of false brinelling and fretting corrosion, Tribology International, 126, 2018.

Schwack, F., Schneider, V., Wandel, S., de la Presilla, R. J., Poll, G., and Glavatskih, S.: On the critical amplitude in oscillating rolling element bearings. 163(107154), 2021.

Schwack, F., Stammler, M., Poll, G., and and Reuter, A.: Comparison of Life Calculations for Oscillating Bearings Considering Individual Pitch Control in Wind Turbines. 753(11), 2016.

Serrano, J., Lacal, R., and Serrano, J.: Technological evolution of onshore wind turbines, a market-based analysis. Wind Energy Science, 19. https://doi.org/10.1002/we.1974, 2016.

Stammler, M.: Wear test programs for roller-type pitch bearings of wind turbines, Wind Energy Science, 2023.

Stammler, M., and Geibel, M.: Results of wear endurance runs of wind turbine pitch, Fraunhofer IWES, Large Bearing Laboratory, Am Schleusengraben 22, D-21029 Hamburg, 2024.

Stammler, M., Menck, O., and Keller, J.: Wind Turbine Design Guideline DG03: Yaw and Pitch Bearings. Technical Report, NREL/TP-5000-89161, 2024.

Stammler, M., Poll, G., and Reuter, A.: The influence of oscillation sequences on rolling bearing wear. Bearing world journal(19–25), 2019.

Wandel, S., Bartschat, A., Glodowski, J., and Bader, N.: Wear Development in Oscillating Rolling Element Bearings. Lubricants, 2023.

Zhu, M. H., Yu, H. Y., and Zhou, Z. R.: Radial fretting behaviours of dental ceramics. 39(10), 2006.

Zuheir, S., Abdullah, O. I., and Al-Maliki, M.: Stress and vibration analyses of the wind turbine blade (A NrEL 5MW),". 42(4), 2019.

APENDIX A

$$a^* = \left(\frac{2 \cdot \varkappa^2 \cdot \xi}{\pi}\right)^{\frac{1}{3}}, \tag{31}$$

$$b^* = \left(\frac{2 \cdot \xi_i}{\pi \cdot \varkappa_i}\right)^{\frac{1}{3}}, \tag{32}$$

$$K = \frac{2^{2/3}}{3 \cdot \delta^* \cdot (1 - v^2) * (S\rho)^{2/3}}, \tag{33}$$

where, E is the elastic modulus of the material, v is the Poisson´s ratio, S_ρ is the sum of the contact curvatures, and δ^* is the dimensionless contact deformation.

475   The sum of the contact curvatures is calculated as:

$$S_\rho = \frac{1}{r_w} + \frac{1}{r_w} \pm \frac{cos(\alpha)}{r_{pw} \pm r_w \cdot cos(\alpha)} \pm \frac{1}{r_p}, \tag{34}$$

where, r_b is the ball radius, r_{pw} is the main bearing radius, r_p is the raceway radius, α is the contact angle, and the sing of both terms is taken as positive for the outer contact and negative for the inner contact.

The dimensionless contact deformation is calculated as:

$$\delta^* = \left(\frac{4 \cdot F^3}{\pi^2 \cdot k^2 \cdot \xi}\right)^{1/3}, \tag{35}$$

where, $\varkappa$ is the elliptical parameter of second kind, ξ is the elliptical parameter of the first kind, and F is the elliptical parameter

480   of second kind, calculated respectively as:

$$\varkappa_i = \rho^{\frac{2}{\pi}}, \tag{36}$$

$$\xi_i = 1 + \frac{\pi - 1}{2 \cdot \rho}, \tag{37}$$

$$F = \frac{\pi}{2} + \left(\frac{\pi}{2} - 1\right) \cdot \ln(\rho), \tag{38}$$

where ρ, is the radius ratio, calculated as:

$$\rho = \frac{4 \cdot r_{pw} \cdot c \cdot r_w}{r_w \cdot (2 \cdot c - 1) \cdot \left(r_{pw} \pm r_w \cdot cos(\alpha)\right)}, \tag{39}$$

and c, is the conformity aspect ratio $c = 2r_p/r_b$, and the sign is considered positive for the outer contact and negative for the inner contact.

485 **Nomenclature**

Abbreviations

IR	Inner ring
OR	Outer ring
FEM	Finite element model
490 CoF	Coefficient of friction
TI	Time increment
TFE	Total accumulated friction energy
MDFE	Maximum density of friction energy
DLC	Design load case
495 DFE | Density of the friction energy |

Symbols

a	Contact ellipse major semi-axes
a_0	Distance from a point to the ellipse edge in the x
500 a^*	Dimensionless mayor semiaxes
b	Contact ellipse minor semi-axes
b_0	Distance from a point to the ellipse edge in the y
b^*	Dimensionless minor semiaxes
C	Creepage coefficient
505 c	Conformity aspect ratio
E	Elastic modulus of the material
E_F	Dissipated friction energy
$\dot{E}_F,$	Rate of dissipated friction energy
E_R	Rolling energy
510 F	Elliptical parameter of second kind
G	Shear modulus
K_i	Stiffness of the inner contact
K_o	Stiffness of the outer ring
k_w	Coefficient of wear
515 k_A | Activation energy threshold |

	L	Flexibility parameter
	M_x	Moment component x at bearing
	M_y	Moment component y at bearing
	P	Contact pressure
520	Q	The reaction force at the ball contact
	r_w	Radius of the ball
	r_{pw}	Bearing pitch diameter
	$r_{e,i}$	Cross-sectional groove radius, e for the outer, and i for the inner ring
	r_0'	Initial effective radius
525	r'	Effective radius
	$\vec{S}$	Local sliding
	S_ρ s	Sum of the contact curvatures
	$\vec{T}$	Tangential stresses
	t	Time
530	t_c	Critical time for wear initiation
	t_s	Time series duration
	v	Poisson´s ratio
	V_w	Wear volume
	$\vec{W}$	Local rigid slip
535	W^{NL}	Local rigid slip of the normal load
	W^{Ro}	Local rigid slip of the rolling effects.
	x', y'	Local coordinate system directions
	z	Number of balls
	ε	Rolling creepage
540	T_1	Traction limits of the contact
	$\vec{U}$	Local elastic slip
	α	Contact angle
	β	Angular movement in transversal direction
	ρ_F	Density of friction energy
545	δ^*	Dimensionless contact deformation
	$\varkappa$	Elliptical parameter of second kind
	ξ	Elliptical parameter of the first kind

	μ	Value of the CoF
	$μ_{tc}$	Mean value of the critical time between series
550	$σ_{tc}$	Deviation of the critical time between series
	$Φ_X$	Probability function of the normal distribution
	X	Density of normal probability distribution1